polymers

MDPI

Article

Polyurea–Graphene Nanocomposites—The Influence of Hard-Segment Content and Nanoparticle Loading on Mechanical Properties

Demetrios A. Tzelepis [1,2], Arman Khoshnevis [3], Mohsen Zayernouri [3,4] and Valeriy V. Ginzburg [1,*]

[1] Department of Chemical Engineering and Materials Science, Michigan State University, East Lansing, MI 48824, USA; tzelepi1@msu.edu
[2] Materials Division, US-Army, Ground Vehicle System Center, Warren, MI 48397, USA
[3] Department of Mechanical Engineering, Michigan State University, East Lansing, MI 48824, USA; khoshne1@msu.edu (A.K.); zayern@msu.edu (M.Z.)
[4] Department of Statistics and Probability, Michigan State University, East Lansing, MI 48824, USA
* Correspondence: ginzbur7@msu.edu

Abstract: Polyurethane and polyurea-based adhesives are widely used in various applications, from automotive to electronics and medical applications. The adhesive performance depends strongly on its composition, and developing the formulation–structure–property relationship is crucial to making better products. Here, we investigate the dependence of the linear viscoelastic properties of polyurea nanocomposites, with an IPDI-based polyurea (PUa) matrix and exfoliated graphene nanoplatelet (xGnP) fillers, on the hard-segment weight fraction (HSWF) and the xGnP loading. We characterize the material using scanning electron microscopy (SEM) and dynamic mechanical analysis (DMA). It is found that changing the HSWF leads to a significant variation in the stiffness of the material, from about 10 MPa for 20% HSWF to about 100 MPa for 30% HSWF and about 250 MPa for the 40% HSWF polymer (as measured by the tensile storage modulus at room temperature). The effect of the xGNP loading was significantly more limited and was generally within experimental error, except for the 20% HSWF material, where the xGNP addition led to about an 80% increase in stiffness. To correctly interpret the DMA results, we developed a new physics-based rheological model for the description of the storage and loss moduli. The model is based on the fractional calculus approach and successfully describes the material rheology in a broad range of temperatures (−70 °C–+70 °C) and frequencies (0.1–100 s^{-1}), using only six physically meaningful fitting parameters for each material. The results provide guidance for the development of nanocomposite PUa-based materials.

Keywords: polyurea; nanocomposite; graphene; elastomer; adhesive; DMA; SEM; fractional Maxwell model

Citation: Tzelepis, D.A.; Khoshnevis, A.; Zayernouri, M.; Ginzburg, V.V. Polyurea–Graphene Nanocomposites—The Influence of Hard-Segment Content and Nanoparticle Loading on Mechanical Properties. *Polymers* **2023**, *15*, 4434. https://doi.org/10.3390/polym15224434

Academic Editor: Alexander Malkin

Received: 6 October 2023
Revised: 10 November 2023
Accepted: 13 November 2023
Published: 16 November 2023

1. Introduction

Polyurethanes (PUs), polyureas (PUas), and poly(urethaneureas) (PUUs), represent a class of polymers with a wide variety of applications [1–4]. Understanding the structure–property–performance relationship is critical in designing materials for specific applications. Critical parameters include the chemical structure of polymer constituents, extent of hydrogen bonding, and volume fraction of hard and soft segments [5–12]. In general, these classes of polymers are produced from a reaction between polyisocyanate (typically a diisocyanate) and a polyol in the case of pure PU and a polyamine in the case of pure PUa and both polyol and polyamine for PUU. In PUa, which will be the focus of this paper, the reaction of the diisocyanate and a polyamine forms the hard segments that have strong bidentate hydrogen bonds [1]. PUa can then be thought of as a multiblock copolymer in which the soft segment blocks alternate with the hard segment blocks. The strong hydrogen bonding within the hard segments drives microphase separation from the soft segments,

resulting in a two-phase system—a percolated hard phase, consisting entirely of the hard segments, and a soft phase, consisting of the soft segments along with small amounts of non-percolated hard segments [10]. This microphase separation is similar to that of classical block copolymers, where various soft-crystalline phases (spherical, cylindrical, lamellar, etc.) are seen for different values of composition, f, and segregation strength, χN [13–15]. The morphology of the polymer, especially the total volume and the connectivity of the hard phase, has a decisive impact on the overall material properties (mechanical, transport, and thermophysical) [10,16–18].

Much of the PU and PUa literature has concentrated on the linear elasticity and especially the "temperature sweep" dynamic mechanical analysis (DMA), where the storage and loss moduli are measured as functions of temperature at a constant frequency (usually 1 Hz). However, many applications (automotive, electronics, etc.) require a good understanding of material performance in a wide range of temperatures and frequencies/strain rates. Thus, recently, Tzelepis et al. [19] used both temperature-sweep and frequency-sweep DMA to study the properties of PUa elastomers with different hard-segment weight fractions (HSWF). It was shown that the studied PUa materials obeyed the time–temperature superposition (TTS) principle. (We note that the application of TTS to PU and PUa was discussed earlier, e.g., by Velankar and Cooper [20] and Ionita et al. [21], but whether it is universally applicable to all PUs and PUas is still uncertain). The TTS shift factor, a_T, was successfully described using the TS2 function [22] that combines Arrhenius temperature dependence at high temperatures with a strong, but non-divergent, increase near the glass transition temperature. The storage and loss modulus master curves showed broad transition regions, indicating a wide distribution of relaxation times. Tzelepis et al. found that such a distribution was well-described by the so-called fractional Maxwell model (FMM) [23–29]—or, to be more precise, a sum of two fractional Maxwell gels (FMG), with one FMG element describing the continuous soft phase (with dispersed hard domains and dissolved hard segments) and the second FMG element representing the percolated hard phase. The plateau modulus of the first element was found to be nearly independent of the HSWF, while the plateau modulus of the second element was a strong function of HSWF, consistent with earlier experiments and theories [10].

In this study, we extend our previous work to investigate a set of PUa nanocomposites with exfoliated graphene nanoplatelets (xGnP), varying both HSWF and the xGnP weight fraction. The use of nanofillers, such as clay, talc, graphene, and graphene oxide, to modify the properties of polymers has been widespread since at least the 1980s [30–41]. The fillers are expected to significantly increase the modulus and strength of the material relative to the "neat" matrix polymer. For high-aspect-ratio nanoplatelets in rubbery polymers, the "reinforcement factor" (RF)—defined as the ratio of the nanocomposite modulus to the matrix modulus—can be as high as 2–4 at particle loadings of 1–4 weight percent [42,43]. Multiple models have been developed to predict reinforcement in simple two-component nanocomposites [42–44]. In general, the stiffness of the material increases strongly at the beginning, but often stays constant or even decreases as the filler loading is increased further—this is typically ascribed to the onset of nanofiller aggregation. Obviously, the problem becomes even more challenging when the matrix itself is multicomponent, like segmented polyurea. Are the nanofillers simply interacting with the pre-set domain nanostructure? Or are they modifying the arrangement of the hard domain itself—perhaps by nucleating their formation or by linking multiple domains? Here, we will attempt to address this problem by preparing multiple PUa-xGnP nanocomposites and investigating their structure and linear viscoelasticity. Starting with three neat PUa materials (20, 30, and 40 percent hard segment), we added xGnP nanofillers, with the xGnP weight percentage (wt%) varying from 0 to 1.5 wt% with increments of 0.5 wt%. We expected that this experimental design would capture the main reinforcement effect due to the nanofillers. On one hand, reinforcement effects are unlikely to be significant at loadings below 0.5 wt%, based on many earlier polymer nanocomposite studies (see, e.g., Pinnavaia and Beall [45]). On the other hand, as it will be seen later, at loadings of 1.5 wt% and above, the reinforcement

effects diminish, possibly due to the nanoparticle interactions and transition from a fully to partially exfoliated morphology. For all twelve materials (neat PUa and nanocomposites), we measured the linear viscoelasticity and successfully fit it with the two-FMG model. The model parameters were then used to elucidate the structural details of the material and provide guidance for the impact of the design parameters (HSWF and wt% xGnP) on the nanocomposite properties.

2. Materials and Methods

2.1. Polymer Synthesis

The synthesis of the PUa-Neat materials is described in detail in our earlier paper [19]. We used isophorone diisocyanate (IPDI)-Vestanat from Evonik Corporation, Pisca-taway, NJ, USA; Jeffamine T5000 and D2000 polyetheramines from the Huntsman Corporation, The Woodlands, TX, USA; and the diethyltoluene diamine (DETDA) (Lonzacure) chain extender from Lonza, Morristown, NJ, USA. Toluene was purchased from Fisher Scientific, Hampton, NH, USA. All the materials were employed in our research "as received", with no further processing. The formulations for the three neat PUa-s having hard segment weight fractions of 20%, 30%, and 40%, are provided in Table 1. We produced polyurea prepolymer (A-side) by placing IPDI in the reactor, then adding toluene to prevent any possible gelling. Next, the amine blend for the prepolymer (comprised of Jeffamine D2000 and T5000) was mixed for 5 min in a separate 250 mL beaker at room temperature, subsequently degassed for approximately 10 min, and added to the IPDI–toluene mixture. Similarly, the amine blend for the B-side, comprised of Jeffamine D2000 and Lonzacure DETDA, was mixed for 5 min in a separate 250 mL beaker followed by vacuum degassing for approximately 10 min and then poured into a separate additional funnel. The reactor was assembled and then a vacuum was drawn for five minutes, followed by the addition of N_2 gas at a 0.3–0.4 L/min flow rate. The reactor temperature was increased to 80 °C and then A-side amine blend was added dropwise under mechanical stirring at 120 RPM. The mixture was subsequently stirred for another hour at 80 °C. Afterward, the reactor was cooled to 0 °C and the B-side amine blend was added dropwise, with mechanical stirring maintained at 120 RPM. Once all the B-side was added, the contents of the reactor were transferred into a 600 mL beaker, degassed for 5 min, and poured into molds. The molds were maintained at room temperature for 24 h to allow for gelation and solvent evaporation. After 24 h, the samples were placed in an oven at 40 °C for 12–24 h to accelerate the solvent evaporation. The curing of the PUa was then completed at 60 °C for 72 h.

Table 1. Summary of the constituents used in the synthesis of the model PUa-Neat. (Adapted with permission from Ref. [19]).

	Component	IPDI-2k-20HS	IPDI-2k-30HS	IPDI-2k-40HS
Isocyanate Prepolymer (A-Side)	IPDI	30.8 g	41.6 g	52.1 g
	T5000	14.5 g	12.1 g	10.1 g
	D2000	57.1 g	48.5 g	40.4 g
	Toluene	82.7 g (95 mL)	165.3 g (190 mL)	208.8 g (240 mL)
	%NCO	8.7%	12.9%	15.3%
Amine Blend (B-Side)	DETDA	10 g	19.4 g	29.3 g
	D2000	90 g	80.6 g	70.7 g

For each of the three PUa formulations described in Table 1, four nanocomposites were then prepared, with the xGnP weight percentage (wt%) varying from 0 to 1.5 wt% with increments of 0.5 wt%. For all the PUa-GnP nanocomposites, the process was identical to that for the neat systems with the following additional steps. Exfoliated nano-graphene (grade R-10, obtained from XG Sciences) was heat-treated at 400 °C for 1 h and allowed to furnace-cool. The required amount of xGnPs was placed in a 500 mL beaker, 190 mL of toluene was added to the beaker, and the slurry was simultaneously mechanically stirred

and sonicated. The mechanical stirring was accomplished by magnetic stirring at 200 rpm. The sonication was accomplished using a Qsonica sonicator, manufac-tured by Qsonica L.L.C, Newtown, CT, USA. The amplitude was set to 20 and the process time was set to 30 min with a pulse time of 10 s on and 10 s off. The temperature of the slurry never exceeded 32 °C, and the total run time was ~1 h. The total amount of energy input was 38,610 J. The weight of xGnP added to the formulation is summarized as follows: for the 0.5 wt% xGnP formulations, 1.02 g of xGnP; for the 1.0 wt% xGnP formulations, 2.04 g of xGnP; and for the 1.5 wt% xGnP formulation, 3.06 g of xGnP.

2.2. PUa–xGnP Characterization

The surface chemistry of the top 50–80 Å was determined with X-ray photoelectron spectroscopy (XPS). The measurements were performed using a PHI 5400 ESCA system. The base pressure of the instrument was less than 10^{-8} Torr. A 1 cm^2 sample was mounted onto the sample holder with double-sided copper tape. The X-ray was a monochromatic Al source with a take-off angle of 45 degrees. Two types of scans were performed for each sample: a survey scan from 0–1100 eV taken with a pass energy of 187.85 eV and regional scans of each element at a pass energy of 23.70 eV. The data were fitted using the CASA XPS software package, version 2.3.15.

The xGnP particle size and dispersion were characterized using a Hitachi (Schaumburg, IL, USA) 3700 SEM. The acceleration was set to 5 keV to minimize charging effects. A 2-to-3-nanometer-thick gold coating was sputtered using a Quorum Q150R sputter coater. Geometric measurements of the xGnP were performed utilizing PCI software, version 9.0.

Dynamic mechanical analysis was conducted using a TA Instruments (New Castle, DE, USA) RSA-G2 rheometer. The curing of the polymer was determined by measuring the change in storage modulus with respect to time. All film samples were loaded in tension. Temperature sweeps, at a rate of 3 °C/min, were conducted from −95 °C to a maximum temperature depending on the polyurea formulation hard segment content. Six repeats per formulation were run for the temperature sweeps. The reference temperature for each material was set to equal its glass transition temperature, defined as the maximum of the loss modulus (see Table S1). All TTS shifts were completed with TA Instruments' TRIOS software package, version 5.1.1.46572.

2.3. Modeling

2.3.1. Fractional-Order Maxwell Gel Model

The Fractional Maxwell Model (FMM) can be employed in developing constitutive models for both soft solids and complex fluids. The FMM consists of two spring-pot elements in series, which describe the complex modulus, E^*, as presented in Equation (1) [25].

$$\frac{E^*(\omega)}{E_o} = \frac{(i\omega\tau_c)^{\alpha}}{1+(i\omega\tau_c)^{\alpha-\beta}} \tag{1}$$

where E_0 represents the characteristic modulus, τ_c denotes the characteristic relaxation time, and both α and β are fractional-order power-law exponents. The storage, E', and loss, E'', moduli were obtained by splitting the complex modulus into its real and imaginary components, respectively defined as

$$\frac{E'(\omega)}{E_o} = \frac{(\omega\tau_c)^{\alpha}\cos\left(\frac{\pi\alpha}{2}\right)+(\omega\tau_c)^{2\alpha-\beta}\cos\left(\frac{\pi\beta}{2}\right)}{1+(\omega\tau_c)^{\alpha-\beta}\cos\left(\frac{\pi(\alpha-\beta)}{2}\right)+(\omega\tau_c)^{2(\alpha-\beta)}} \tag{2a}$$

$$\frac{E''(\omega)}{E_o} = \frac{(\omega\tau_c)^{\alpha}\sin\left(\frac{\pi\alpha}{2}\right)+(\omega\tau_c)^{2\alpha-\beta}\sin\left(\frac{\pi\beta}{2}\right)}{1+(\omega\tau_c)^{\alpha-\beta}\cos\left(\frac{\pi(\alpha-\beta)}{2}\right)+(\omega\tau_c)^{2(\alpha-\beta)}} \tag{2b}$$

Within the FMM framework, one possible special case that can occur is the fractional Maxwell gel (FMG), denoted by β being set to 0, which models the material's elastic behavior past the gel point.

In our model of interest, two FMG elements were arranged in parallel, representing the *soft-phase* matrix and percolated *hard phase* of polyurea, as illustrated in Figure 1. Given the relatively low mass fraction of the added nanoparticles (only up to 1.5%), we assumed that they were ultimately dispersed within the two phases and not forming a new phase by themselves. Thus, no additional parallel branch was introduced, consistent with our prior work [19]. Consequently, each polymer was characterized by six model parameters, encompassing two characteristic moduli (often called plateau modulus) ($E_{0,1}$ and $E_{0,2}$), two relaxation characteristic times ($\tau_{c,1}$ and $\tau_{c,2}$), and two power-law exponents (α_1 and α_2). We expect these parameters—especially those related to the percolated hard phase (FMG2)—to depend on the material formulation, including HSWF and xGnP loading.

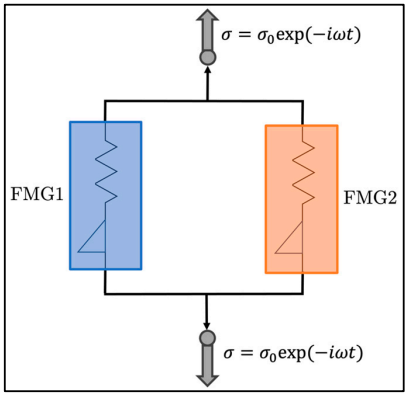

Figure 1. Schematic illustration of the two FMGs employed to model the polyurea. FMG1 represents the filled soft phase, whereas FMG2 corresponds to the percolated hard phase. No additional FMG element was considered for modeling nano-particles. Each FMG comprised an elastic spring and a spring-pot in a series arrangement.

To integrate the DMA data across various temperatures, the time–temperature superposition (TTS) principle was employed and the shift factor, denoted as a_T, was assumed to hold the same for both the soft and hard phases. As a result, the master curves could be described through the following equations:

$$E'(x) = \sum_{k=1}^{2} E_{0,k} \frac{(x\tau_k)^{\alpha}\cos\left(\frac{\pi\alpha}{2}\right) + (x\tau_k)^{2\alpha}}{1 + (x\tau_k)^{\alpha}\cos\left(\frac{\pi\alpha}{2}\right) + (x\tau_k)^{2\alpha}} \tag{3a}$$

$$E''(x) = \sum_{k=1}^{2} E_{0,k} \frac{(x\tau_k)^{\alpha}\sin\left(\frac{\pi\alpha}{2}\right)}{1 + (x\tau_k)^{\alpha}\cos\left(\frac{\pi\alpha}{2}\right) + (x\tau_k)^{2\alpha}} \tag{3b}$$

where $x = a_T\omega$. The equation for the shift factor as a function of temperature is discussed next.

2.3.2. The Shift Factor and the Two State, Two (Time) Scale (TS2) Model

In our previous paper [19], we applied three different functional forms to describe the shift factor—the Arrhenius, the Williams–Landel-Ferry (WLF) [46], and the TS2 [22] functions. The TS2 model describes the glass transition as the transition between the high-temperature and low-temperature Arrhenius regions,

$$ln(a_T) \equiv ln\left(\frac{\tau[T]}{\tau[T_o]}\right) = \frac{E_1}{RT} + \frac{E_2 - E_1}{RT}\left(\frac{1}{1 + exp\left\{\frac{\Delta S}{R}\left(1 - \frac{T^*}{T}\right)\right\}}\right) - \frac{E_1}{RT_o} + \frac{E_2 - E_1}{RT_o}\left(\frac{1}{1 + exp\left\{\frac{\Delta S}{R}\left(1 - \frac{T^*}{T_o}\right)\right\}}\right) \tag{4}$$

where E_1 and E_2 are activation energies (in J/mol), $\Delta S/R$ is the dimensionless transition entropy between the solid and liquid states of matter, T^* is the transition temperature (K) (typically, $T^* \approx T_g$), and T_o is the reference temperature of the TTS shifts. Equation (4) was shown to successfully describe the TTS of neat PUa polymers in the temperature range between −70 °C and +70 °C [19] and thus will be utilized here as well.

2.3.3. Optimization of the FMG Parameters

A global particle-swarm optimization (PSO) algorithm [47] was utilized to infer the fitting parameters in the two FMG branches, depicted in Figure 1. This is the same method that was employed in our previous paper [19]. Each optimization run maintained a constant population size of $N_{pop} = 200$ and performed $N_{it} = 6000$ iterations. Given the stochastic nature of the PSO algorithm, 50 optimization runs were conducted, and the expected values and standard deviations for each parameter of materials are reported.

The following parameter ranges are considered for all samples (20%, 30%, and 40% HS, with 0, 0.5%, 1%, and 1.5% GnP). The characteristic moduli are confined to the ranges of $0 \leq E_{0,1} \leq 10^4$ MPa and $0 \leq E_{0,2} \leq 10^3$ Mpa, the characteristic times are confined to the range of 10^{-3} s $\leq \tau_{c,1(2)} \leq 10^2$ s, and the fractional power law exponents α_1 and α_2 span from 0 to 1.

Equation (5) establishes a scalar multi-objective cost function via a weighted summation for the simultaneous fitting of storage and loss moduli.

$$\underset{\theta}{\text{Min}} \omega_1 f_1(\theta) + \omega_2 f_2(\theta) \tag{5}$$

where θ denotes the vector of fitting parameters, with $\omega_1 = 1/2$ and $\omega_2 = 1/2$, and the cost functions corresponding to both moduli are provided as follows:

$$\begin{aligned} f_1(\theta) &= \sum_{i=1}^{N_d} \left(\text{Log}\left(\frac{E'_{exp}}{E'_{model}}\right) \right)^2, \\ f_2(\theta) &= \sum_{i=1}^{N_d} \left(\text{Log}\left(\frac{E''_{exp}}{E''_{model}}\right) \right)^2 \end{aligned} \tag{6}$$

where N_d is the number of data points where our model is evaluated. The decision to employ a logarithmic difference between experimental data and model predictions arises from the significant variations in orders of magnitude for the storage and loss moduli across decades of frequency ranges. Moreover, the quality of the two-branch FMG model fits, if assessed by the relative error, is defined in Equation (7).

$$error = \frac{\omega_1 f_1(\theta) + \omega_2 f_2(\theta)}{\omega_1 \sum_{i=1}^{N_d} \left(\text{Log}\left(E'_{exp}\right) \right)^2 + \omega_2 \sum_{i=1}^{N_d} \left(\text{Log}\left(E''_{exp}\right) \right)^2} \tag{7}$$

Both the two-branch FMG model and PSO codes—similar to our previous paper [19]—were developed in MATLAB R2021b and executed in ICER MSU HPCC system with 1 node, 24 CPU, and 48 GB RAM.

Once again, we selected the GRG non-linear engine and imposed the following constraints: (1) E_1 < 130 kJ/mol, (2) E_2 < 350 kJ/mol, (3) $\Delta S/R$ < 25, and (4) T^* < 350 K. The reference temperature (T_o) was set to match the glass transition temperature, defined as the maximum of the loss modulus (−60 ± 5 °C; for more details, see Table S1). The minimization function utilized is the average absolute value of the difference in the natural logarithm of the experimental and model shift factors, as defined in Equation (8).

$$\overline{error} = \left| ln\left(aT_{exp}\right) - ln\left(aT_{model}\right) \right| \tag{8}$$

This concludes the discussion of materials and methods; we now turn to the results.

3. Results

3.1. Experimental Results

Scanning electron microscopy (SEM) was used to determine the effect of sonication on the xGnP. Figure S1 shows SEM micrographs at various magnifications. Estimates of the particle diameter were produced by measuring the longest axis of the platelets, as shown in Figure S2. The average particle diameter before sonication was 15.4 +/− 6.3 μm (1σ). The average particle diameter after sonication was 15.0 +/− 4.5 μm (1σ). No change was seen in the morphology of the xGnP. The xGnP remained exfoliated throughout the sonication process and retained their shape and aspect ratio. Given that the technical data sheet for the R10 grade specified an average particle diameter size of approximately 10 μm, and accounting for the fact that the platelets in the images were at various angles, we conclude that there was no difference between the as-received and sonicated xGnP.

X-ray photoelectron spectroscopy (XPS) was used to evaluate the surface chemistry of the xGnP after heat treatment and after sonication. Figure 2 shows a survey of both a heat-treated sample and heat-treated and sonicated sample. Both spectra showed two peaks. The first at 281.6 eV and 282.4 eV for the heat-treated and sonicated samples, respectively, are associated with the C 1s position. The second at 530.4 eV for both heat-treated and sonicated samples is associated with the O 1s position. The atomic concentration was estimated and is presented in Figure 2.

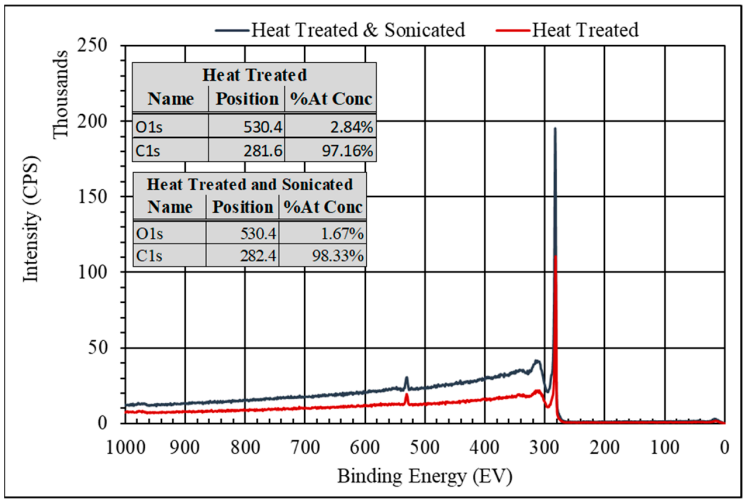

Figure 2. XPS survey of the xGnP after heat treatment (red spectrum), and after heat treatment and sonication. The sonication did not cause any change to the surface chemistry of the xGnP.

The atomic percentage of C was significantly higher than that of O for both heat-treated and heat-treated and sonicated samples. This is consistent with the expectation that the majority of the xGnP was carbon with very little oxygen-based functionalization on the edges of the basal plane. The approximate 1% difference seen between the two treatments was not considered significant. In order to explore the source of the oxygen peaks, a deconvolution of the XPS spectra for the heat-treated sample and the heat-treated and sonicated sample in the binding energy region for C and O is shown in Figure S3 and Figure S4, respectively. From Figure S3a, the peak at 283.2 eV, the largest peak, was associated with the C=C double bonds of graphene. The remaining C 1s peaks were associated with hydroxyl 284.7 eV. The C 1s peak at 288.0 eV was associated with the C=O, and the C 1s peak at 289.7 was associated with a COOH/COOR [48]. From Figure S3b, the O 1s peak at 531.2 eV was associated with COOH and the O 1s peak at 532.7 eV was associated with the –OH functional group [49]. The deconvolution of the heat-treated and sonicated samples is shown in Figure S4. Similar to the analysis for the heat-treated samples, the peak at 283.2 eV (the largest peak in the spectrum) was associated with the C=C double bonds of graphene.

The remaining C1s peak at 284.7 eV was associated with the –OH functional group. Likewise, the C 1s peak at 289.2 eV was associated with COOH/COOR functional groups (see Figure S4a,b). In Figure S4b, the O 1s peak at 531.0 eV was associated with COOH, and the O 1s peak at 532.4 eV was associated with the –OH functional group. From the analysis above, one concludes that there was very little –OH or –COOH functionalization on the xGnP; furthermore, the sonication process had very little effect on the chemistry, nor did it reduce the particle size.

In order to investigate particle dispersion at various concentrations of xGnP, tensile samples were placed in liquid nitrogen for about 5 min and then snapped in half. SEM micrographs of the fracture surface were then used to study the nanoparticle dispersion in the polymer matrix (see Figure 3 and also Figures S5–S7). In the lower-magnification micrographs, the xGnP was brighter, due to electron interaction with the jagged edges of the xGnP, than the polyurea matrix; examples of xGnP are highlighted by the arrows. No agglomeration or continuous networks of xGnP were found in any of the formulations. Figures S5f and S7f are higher-magnification micrographs (13 kX, and 10 kX respectively) of the xGnP. The edges of the individual nano-plates can be seen, suggesting the GnP remained exfoliated throughout the sample preparation process.

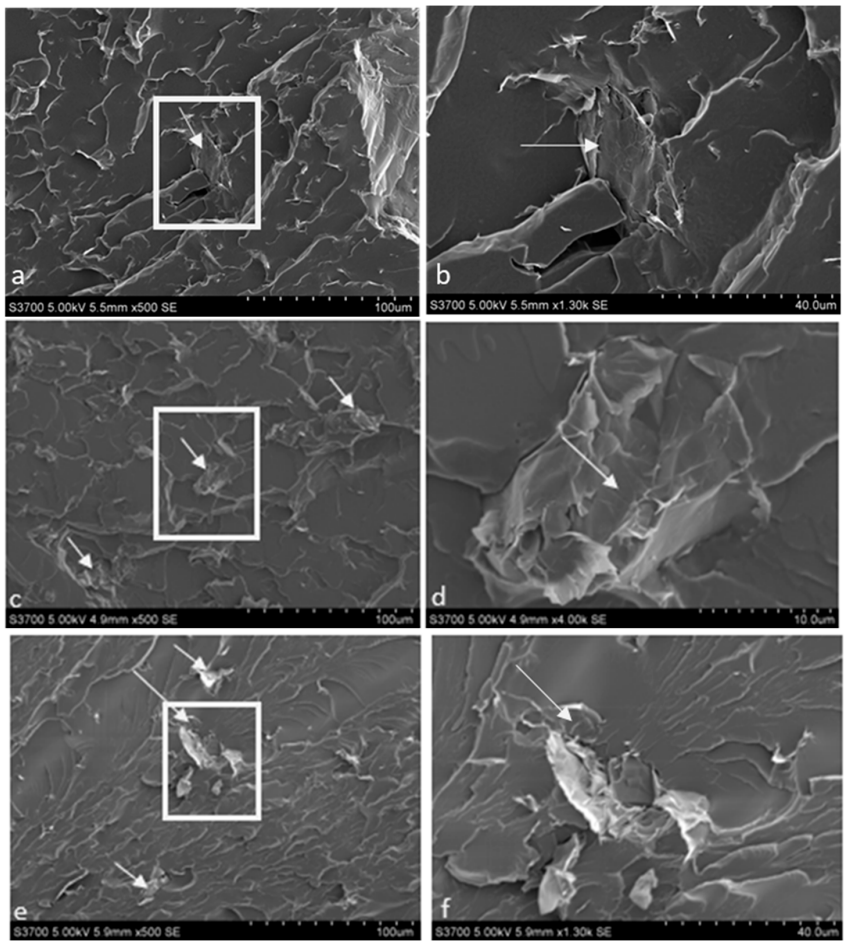

Figure 3. SEM photomicrographs of the fracture surface for PUa-xGnP nanocomposites with 0.5 wt% xGnP loading: (**a**) 20% HSWF at 500×, (**b**) photomicrograph of the white box in (**a**). (**c**) 30% HSWF at 500×, (**d**) photomicrograph of the white box in (**c**). (**e**) 40% HSWF at 500×, (**f**) photomicrograph of the white box in (**e**). In all photomicrographs, the arrows point to the xGnP.

Figure 4 shows the storage modulus curves for the DMA temperature sweeps (frequency 1 Hz) for the (a) IPDI-2k-20HS, (b) IPDI-2k-30HS, and (c) IPDI-2k-40HS formulations at various xGnP loadings. Note that the complete E', E'', and tan(δ) curves for all formulations are shown in the supplemental section, Figures S8–S10. For all formulations, the addition of xGnP did not have an appreciable effect on the T_g (as measured by E', E'' or tan(δ) curves) of the PUa formulations, nor did it have a significant effect on the glassy modulus. For these formulations, the T_g and glassy modulus were determined primarily by the soft phase [19]. This would tend to indicate the xGnP had little effect on the soft-phase microstructure, i.e., no crystallization or increase in the hydrogen bonding in the soft phase. For the IPDI-2k-20HS and IPDI-2k-30HS PUas, the addition of xGnP increased the plateau modulus and the temperature range of the plateau modulus. For the IPDI-2k-40HS formulations, the addition of xGnP had no effect on the temperature sweeps.

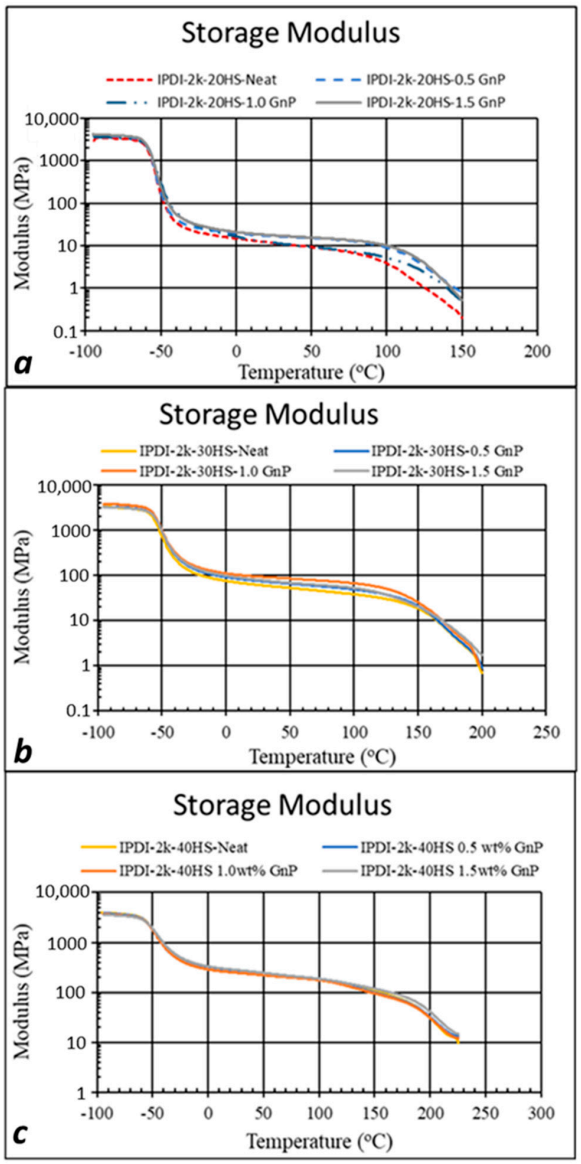

Figure 4. DMA temperature sweeps (tensile storage modulus, E′) showing the effect of both an increase in % HS and an increase in xGnP loading: (**a**) IPDI-2k-20HS with 0, 0.5, 1.0, and 1.5 wt % xGNP; (**b**) the same for the IPDI-2k-30HS polyurea; (**c**) the same for the IPDI-2k-40HS polyurea.

3.2. Modeling Results

As previously discussed, the linear viscoelastic behavior of polyurea was described by a model comprising two parallel fractional Maxwell gel (FMG) branches representing the soft and hard phases. Even though, in the nanocomposites, there was a new phase (xGnPs), we continued to use the two-FMG model and expected that the impact of the nanofillers would be only in modifying the parameters of one or both of the FMGs, at least at sufficiently low loadings (<1.5 wt% in our case). This modeling approach enabled us to effectively capture the broad spectrum of relaxation times seen in these materials. The parameterization process was previously detailed, and we now present the results.

To begin with, in Figure 5, we plot the shift factor as a function of temperature for the IPDI-2k-20HS nanocomposites with (a) 0%, (b) 0.5%, (c) 1%, and (d) 1.5% xGnP. The symbols are the results of the TTS shift of the data (as outlined above), and the lines are the TS2 (Equation (4)) fits. Obviously, the addition of xGnPs did not have a qualitative impact on the TTS or the temperature dependence of the shift factor, although the model parameters (such as activation energies) changed slightly. Similar data and model fits for the IPDI-2k-30HS and IPDI-2k-40HS nanocomposites are presented in Figures S10 and S11, and the TS2 model parameters are summarized in Table S1.

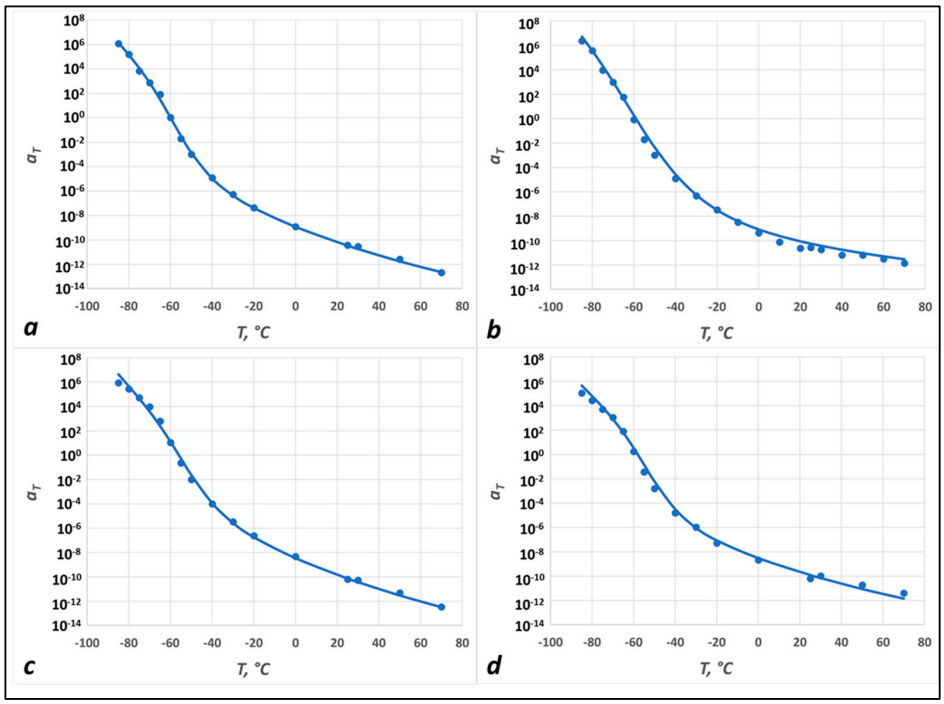

Figure 5. Experimental (symbols) and TS2 fit (lines) shift factors for 20HS polyureas with: (**a**) No added nanofillers; (**b**) 0.5 wt% xGnP; (**c**) 1.0 wt% xGnP; (**d**) 1.5 wt% xGnP.

In Figure 6, the storage and loss master curves are plotted for all nanocomposite systems: (a) IPDI-2k-20HS matrix, (b) IPDI-2k-30HS matrix; and (c) IPDI-2k-40HS matrix. Within each "family", all curves were very close to each other, with a possible exception of the IPDI-2k-20HS, 1% xGnP (blue symbols in Figure 6a). We will return to this system later to discuss the origins of its uniqueness.

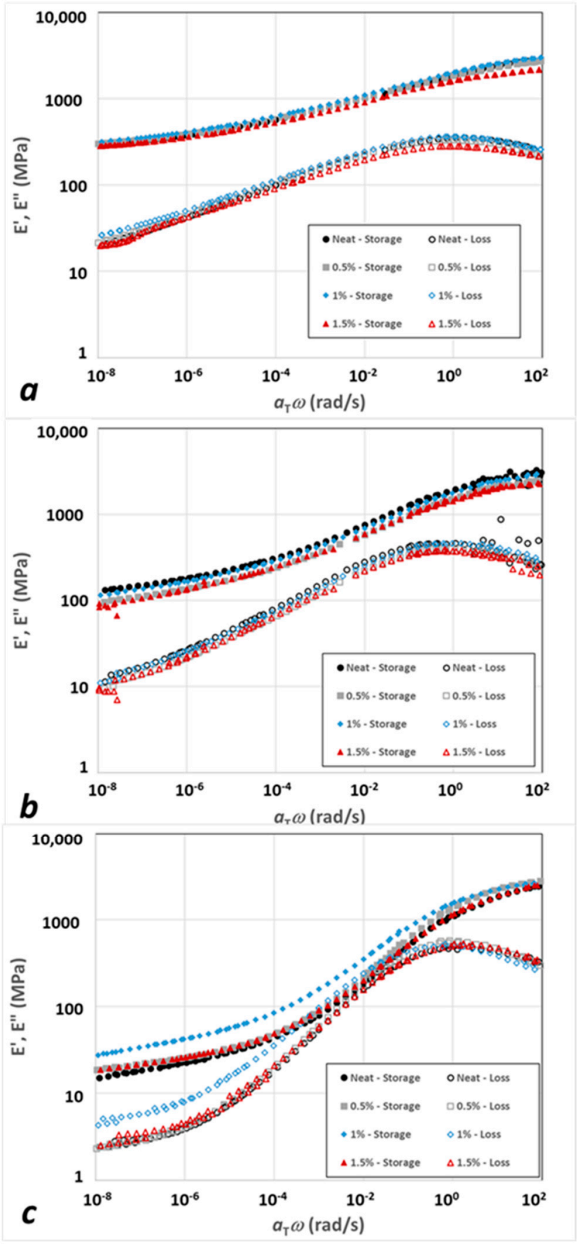

Figure 6. Master curves for the tensile storage (filled symbols) and loss (open symbols) moduli. (**a**) 20HS matrix with 0, 0.5, 1.0, and 1.5 wt % xGnP. (**b**) Same as (**a**) for the 30HS matrix. (**c**) Same as (**a**) for the 40HS matrix.

Next, let us consider the results of the two-FMG fitting to the master curves.

Table 2 provides the mean values and corresponding standard deviations for all six parameters in our two-FMG model. The optimization runs showed excellent convergence and reproducibility, as manifested in the low standard deviation values for all the systems considered.

Figure 7 presents the two-FMG model fits to the experimental shifted data for IPDI-2k-40HS nanocomposites; the results for IPDI-2k-20HS and IPDI-2k-30HS are depicted in Figures S12 and S13, respectively. All fitted curves were generated using the expected values for the model parameters, since the standard deviation of each model parameter

was negligible. For all the formulations, the relative error between the model and data was less than 3.1%, with data spanning a broad range of frequencies (between 10^{-4} and 10^{2} rad/s). However, for the 20 wt% hard segment sample at all nano-particle percentages, a minor deviation between the model and experimental data was observed above the glass transition point in the loss modulus, a phenomenon which was also noted in our prior work for the neat 20% HWSF case. It should be noted that the experimental data points exhibiting a high level of dispersion were excluded from the optimization and fitting process.

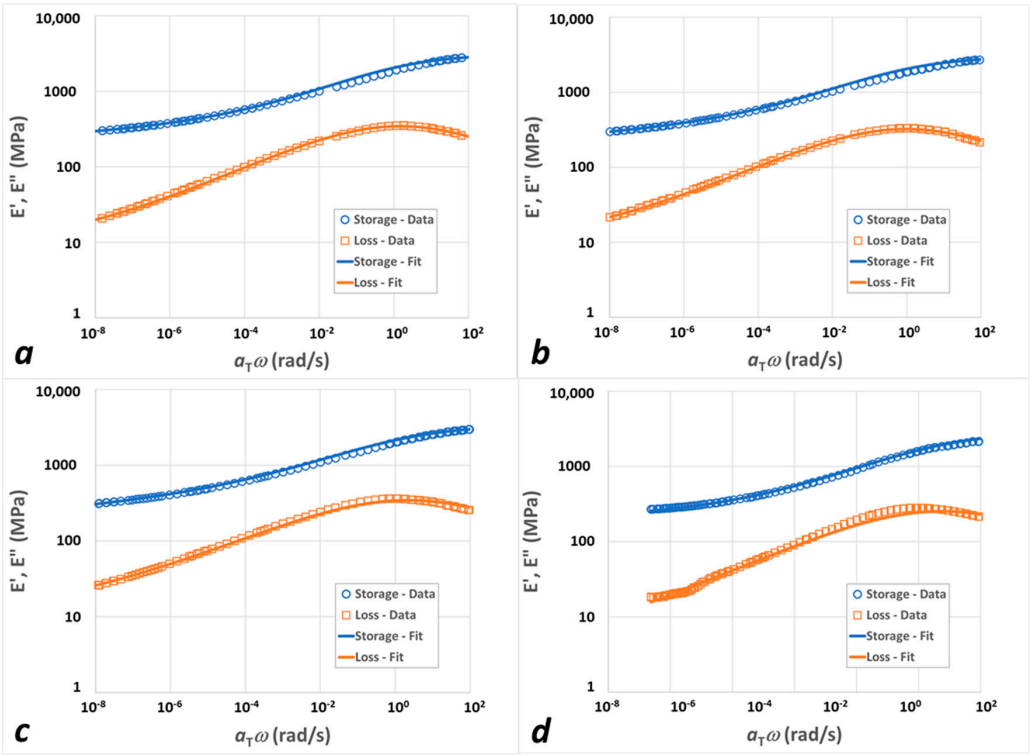

Figure 7. Experimental (symbols) and FMG-FMG fit (lines) master curves for 40HS polyureas with: (**a**) no added nanofillers; (**b**) 0.5 wt% xGnP; (**c**) 1.0 wt% xGnP; (**d**) 1.5 wt% xGnP. Blue open circles represent storage modulus data NS blue lines are the storage modulus model fits; orange open squares correspond to the loss modulus data and orange lines are the loss modulus model fits.

Figure 8a,b depicts the influence of the nanofiller content on the mean characteristic modulus of both branches. In general, the effect was very small, except for the significant increase in $E_{0,2}$ for the 1% xGnP in the IPDI-2k-20HS nanocomposite relative to the neat polymer. In that system, two factors contributed to the effect. First, the stiffness ratio between the filler and the matrix was the largest for the lower-HS polymers and became smaller as HSWF increased. Second, the impact of the fillers usually had a maximum as a function of filler loading. At low loadings, the effect was, obviously, very weak; at high loadings, on the other hand, the platelets aggregated, the aspect ratio decreased, and the overall effect decreased as well. Thus, 1% xGnP in the IPDI-2k-20HS represented the system corresponding to the maximum reinforcement in terms of both HSWF and %xGnP.

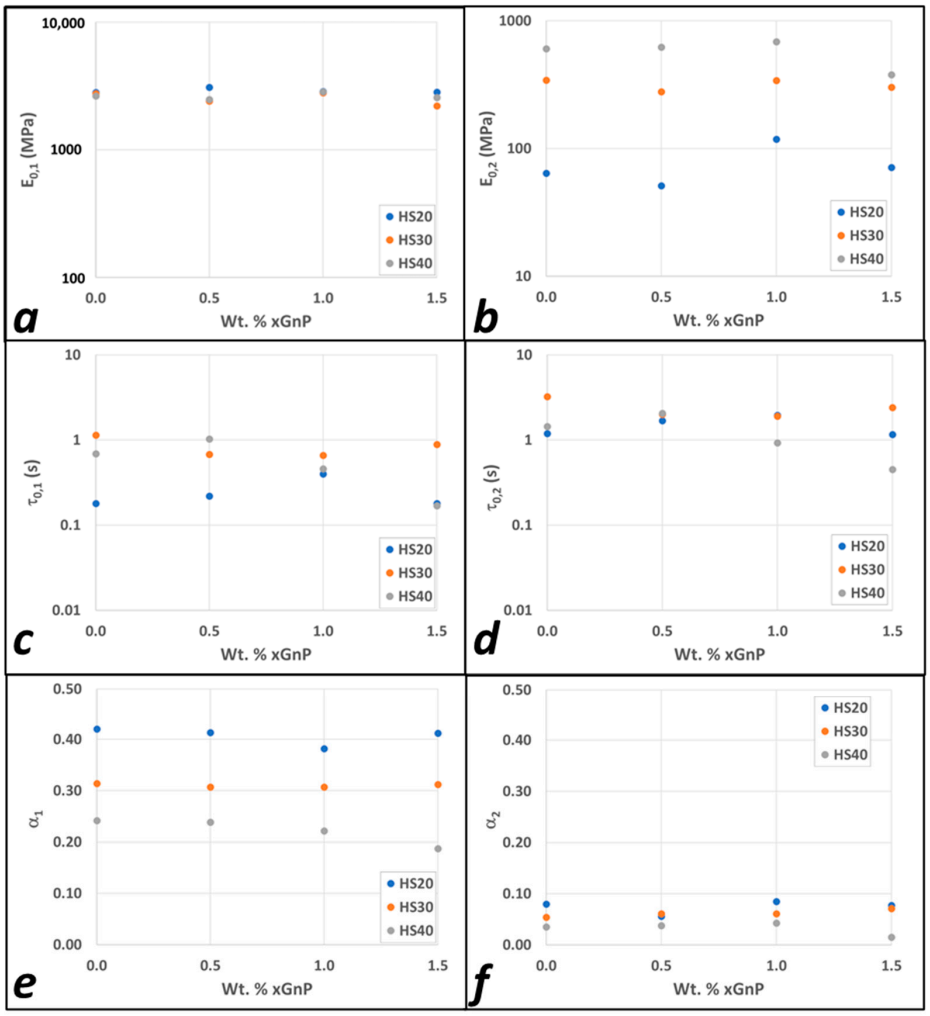

Figure 8. Effect of the nanofiller loading on the (**a**) characteristic modulus of the first branch ($E_{0,1}$) (**b**) characteristic modulus of the second branch ($E_{0,2}$), (**c**) characteristic time of the first branch ($\tau_{c,1}$), (**d**) characteristic time of the second branch ($\tau_{c,2}$), (**e**) power law exponent of the first branch (α_1), and (**f**) power law exponent of the first branch (α_2).

In Figure 8c,d, the variations in relaxation times for both branches with respect to the filler weight fraction are shown. These variations are also fairly small and do not show a clear dependence on the nanoparticle loading. Finally, Figure 8e,f shows the power law exponents, α, for both branches. Again, the dependence of α_I on the xGnP loading was fairly weak. The soft-phase exponent, α_1, showed a strong dependence on HSWF, decreasing as HSWF increased. This is consistent with the material becoming "more elastic" and the average loss tangent decreasing. The hard-phase exponent, α_2, was quite small for all twelve neat and nanocomposite systems, indicating that they were almost always nearly perfectly elastic.

Table 2. FMG 1 and FMG 2 parameters. Rows represent hard segment weight fractions of 20%, 30%, and 40%, while columns correspond to xGnP weight fractions of 0.0%, 0.5%, 1%, and 1.5%.

Model Parameters		0.0% GnP		0.5% GnP		1% GnP		1.5% GnP	
		FMG 1	**FMG 2**	**FMG 1**	**FMG 2**	**FMG 1**	**FMG 2**	**FMG 1**	**FMG 2**
IPDI-2k 20HS	$E_{0,i}$ (MPa)	2815	64	3097	51	2871	118	2837	71
		$\pm 3.3 \times 10^{-6}$	$\pm 3.8 \times 10^{-7}$	$\pm 3.4 \times 10^{-6}$	$\pm 3.9 \times 10^{-7}$	$\pm 2.6 \times 10^{-6}$	$\pm 6.2 \times 10^{-7}$	$\pm 2.6 \times 10^{-6}$	$\pm 4.1 \times 10^{-7}$
	$\tau_{c,i}$ (s)	0.18	1.19	0.22	1.69	0.40	1.96	0.18	1.16
		$\pm 8.2 \times 10^{-10}$	$\pm 5.9 \times 10^{-10}$	$\pm 6.8 \times 10^{-10}$	$\pm 7.1 \times 10^{-9}$	$\pm 1.4 \times 10^{-9}$	$\pm 8.1 \times 10^{-9}$	$\pm 6.7 \times 10^{-10}$	$\pm 4.5 \times 10^{-9}$
	α_i	0.42	0.080	0.413	0.056	0.382	0.085	0.412	0.077
		$\pm 4.3 \times 10^{-10}$	$\pm 3.8 \times 10^{-10}$	$\pm 4.4 \times 10^{-10}$	$\pm 5.8 \times 10^{-10}$	$\pm 3.5 \times 10^{-10}$	$\pm 3.4 \times 10^{-10}$	$\pm 4.0 \times 10^{-10}$	$\pm 3.9 \times 10^{-10}$
IPDI-2k 30HS	$E_{0,i}$ (MPa)	2757	342	2405	278	2793	341	2203	301
		$\pm 1.8 \times 10^{-5}$	$\pm 1.7 \times 10^{-6}$	$\pm 3.4 \times 10^{-6}$	$\pm 1.5 \times 10^{-6}$	$\pm 2.5 \times 10^{-6}$	$\pm 1.2 \times 10^{-6}$	$\pm 1.9 \times 10^{-5}$	$\pm 8.9 \times 10^{-6}$
	$\tau_{c,i}$ (s)	1.14	3.23	0.68	2.00	0.66	1.90	0.89	2.41
		$\pm 4.1 \times 10^{-8}$	$\pm 1.0 \times 10^{-7}$	$\pm 5.8 \times 10^{-9}$	$\pm 1.2 \times 10^{-8}$	$\pm 2.7 \times 10^{-9}$	$\pm 6.3 \times 10^{-9}$	$\pm 2.7 \times 10^{-8}$	$\pm 3.0 \times 10^{-8}$
	α_i	0.314	0.054	0.307	0.061	0.307	0.061	0.312	0.071
		$\pm 1.1 \times 10^{-9}$	$\pm 3.6 \times 10^{-10}$	$\pm 5.7 \times 10^{-10}$	$\pm 3.4 \times 10^{-10}$	$\pm 3.4 \times 10^{-10}$	$\pm 2.2 \times 10^{-10}$	$\pm 2.5 \times 10^{-9}$	$\pm 2.0 \times 10^{-9}$
IPDI-2k 40HS	$E_{0,i}$ (MPa)	2635	604	2476	622	2843	687	2567	378
		$\pm 2.6 \times 10^{-6}$	$\pm 2.0 \times 10^{-6}$	$\pm 2.0 \times 10^{-6}$	$\pm 1.7 \times 10^{-6}$	$\pm 2.8 \times 10^{-6}$	$\pm 2.8 \times 10^{-6}$	$\pm 1.3 \times 10^{-5}$	$\pm 1.1 \times 10^{-5}$
	$\tau_{c,i}$ (s)	0.69	1.44	1.03	2.06	0.46	0.93	0.17	0.45
		$\pm 2.8 \times 10^{-9}$	$\pm 5.2 \times 10^{-9}$	$\pm 3.4 \times 10^{-9}$	$\pm 8.8 \times 10^{-9}$	$\pm 2.1 \times 10^{-9}$	$\pm 4.9 \times 10^{-9}$	$\pm 2.7 \times 10^{-9}$	$\pm 3.7 \times 10^{-9}$
	α_i	0.242	0.035	0.239	0.038	0.222	0.043	0.187	0.015
		$\pm 4.1 \times 10^{-10}$	$\pm 1.8 \times 10^{-10}$	$\pm 2.8 \times 10^{-10}$	$\pm 1.6 \times 10^{-10}$	$\pm 3.4 \times 10^{-10}$	$\pm 1.8 \times 10^{-10}$	$\pm 1.2 \times 10^{-9}$	$\pm 1.7 \times 10^{-9}$

4. Discussion

In this study, we investigated the structure and linear viscoelasticity of polyurea elastomers to be used in adhesive applications. The two main variables of interest were the polyurea hard segment (HS) weight fraction and the exfoliated graphene nanoplatelet (xGnP) loading. The hypothesis tested was that the polyurea hard segment and the nanofillers would interact strongly with each other and provide additional reinforcement by forming a "combined hard phase".

Using scanning electron microscopy (SEM), we verified that the heat treatment and the sonication in toluene resulted in no morphological changes in the xGnP. The average particle diameter did not change and the xGnPs remained exfoliated and well dispersed in the PUa matrix. Recall that the nanoparticles were placed on the isocyanate side (A-side) of the PUa reaction sequence; therefore, albeit small, there was a potential for the isocyanate to react with any hydroxyl or carboxylic acid functional groups located on the edges of the nano particles. However, XPS showed very few, if any, available reaction sites, whether they be hydroxyl or carboxylic acid that could potentially react with the isocyanate. Thus, we stipulate that the dispersed xGNPs had only weak physical interactions with the PUa matrix.

Given the complex structure of any polyurea nanocomposite (soft-phase matrix, hard-phase islands, percolated hard-phase domains, exfoliated nanofillers, aggregated nanofillers, etc.), the data from direct characterization, such as electron microscopy, are often inconclusive. Thus, here, we also concentrated on understanding the materials using linear viscoelasticity and inferring the information about the matrix–filler interaction from the DMA results.

Similar to the previous study [19], we observed that the DMA frequency sweeps in these systems are amenable to time–temperature superposition (TTS), with the TTS shift factors well-described by the TS2 [22] function. This was, in itself, a non-trivial result, since polyurea materials are multi-phase; understanding the reason why TTS works still requires additional analysis. We also found that the storage and loss master curves exhibited broad transition regions and thus could not be described with a single Maxwell model. Therefore, we used the fractional Maxwell model (FMM) approach [23–27] to quantify the viscoelastic

response and fit the master curve. In particular, the material was well-described by the use of two fractional Maxwell gel (FMG) elements, one representing the soft phase and another one representing the percolated hard phase. We demonstrated that the plateau modulus of the percolated hard phase (FMG2) increased strongly with the hard segment weight fraction (HSWF), consistent with earlier studies [10]. Here, we used the same approach to determine the combined impact of HSWF and xGnP loading.

Based on the FMM analysis, we observed that the effect of the xGnP was significantly less pronounced than the effect of the HSWF change. The reinforcement factor (RF) was physically meaningful (significantly greater than 1) only for one nanocomposite system—HS20 with 1% xGnP. This result is consistent with expectations, as discussed above. Further increases in the xGnP loading likely resulted in at least some aggregation, thus blunting the effectiveness of the new fillers [50]. For polyureas with higher HSWF, the percolated hard-phase modulus is already quite high, and the contribution of the nanofillers becomes even less significant, regardless of their concentration. Thus, the addition of the nanofillers did not seem to offer a significant increase in the linear elastic properties of the polyureas studied here.

Of course, linear elasticity is not the only important property for adhesives—other properties of interest include tensile strength, ultimate elongation, fracture toughness, etc. The influence of nanofillers on those properties will be the subject of future work.

5. Conclusions

We investigated the structure and linear viscoelasticity of polyurea (PUa) elastomers and their nanocomposites with expanded graphene nanoplatelets (xGNPs) as a function of the hard segment weight fraction (HSWF) of the polyurea and the xGNP weight fraction in the overall nanocomposites. Experimentally, we found that the room-temperature modulus of the PUa-xGNP nanocomposites depended strongly on HSWF (about 10 MPa for the 20% HSWF to about 100 MPa for the 30% HSWF and about 250 MPa for the 40% HSWF polymer), but weakly on the xGNP weight fraction (for the weight fraction variations between 0 and 1.5 wt%, the modulus variations were generally within the experimental error, except for the 20% HSWF, 1% xGNP nanocomposite exhibiting nearly two-fold stiffening compared with the neat material).

Significantly, we have demonstrated that, despite their structural complexity, PUa-xGNP nanocomposites exhibit time–temperature superposition (TTS). For the first time, we demonstrated that the TTS master curves can be described by fractional calculus (FC)-based models with a small number of physically meaningful parameters (as opposed to the standard Prony-series modeling usually requiring twenty or more). The new model can be adapted to describe other polymers and nanocomposites for both linear and nonlinear mechanical tests.

Supplementary Materials: The following supporting information can be downloaded at: https://www.mdpi.com/article/10.3390/polym15224434/s1, Figure S1: SEM images at various magnifications of the xGnP before (left column) and after sonication (right column). The images indicate that there was no change in the morphology of the GnP with the sonication parameters used; Figure S2: SEM micrographs showing the measurement of the estimated diameter of the xGnP before sonication (a) and after sonication (b); Figure S3: Deconvolution of the XPS spectrum, for the heat-treated xGnP, in the binding energy region for C (a) and O (b); Figure S4: Deconvolution of the XPS spectrum for the heat-treated and sonicated xGnP and sonicated xGnP in the binding energy regions for C (a) and O (b); Figure S5: SEM photomicrographs of the fracture surface for all IPDI-2k-20HS xGnP loadings: (a) 0.5 wt% xGnP loading at 500×, (b) photomicrograph of the white box in (a). (c) 1.0 wt% xGnP loading at 500×, (b) photomicrograph of the white box in (c). (d) 1.5 wt% xGnP loading; Figure S6: SEM photomicrographs of the fracture surface for all IPDI-2k-30HS xGnP loadings: (a) 0.5 wt% xGnP loading at 500×, (b) photomicrograph of the white box in (a). (c) 1.0 wt% xGnP loading at 500×, (b) photomicrograph of the white box in (c). (d) 1.5 wt% xGnP loading at 650×. Photomicrograph of the white box in (e). In all photomicrographs, the arrows point to the xGnP; Figure S7: SEM photomicrographs of the fracture surface for all IPDI-2k-40HS xGnP loadings: (a) 0.5 wt% xGnP

loading at 500×, (b) photomicrograph of the white box in (a). (c) 1.0 wt% xGnP loading at 500×, (b) photomicrograph of the white box in (c). (d) 1.5 wt% xGnP loading at 650×. Photomicrograph of the white box in (e). In all photomicrographs, the arrows point to the xGnP; Figure S8: DMA temperature sweep showing the storage, loss modulus, and the tan (δ) for the IPDI-2k-20HS; Figure S9: DMA temperature sweep showing the storage, loss modulus, and the tan (δ) for the IPDI-2k-30HS; Figure S10: DMA temperature sweep showing the storage, loss modulus, and the tan (δ) for the IPDI-2k-40HS; Figure S11: Experimental (symbols) and TS2 fit (lines) shift factors for IPDI-2k-30HS polyureas with: (a) no added nanofillers; (b) 0.5 wt% xGnP; (c) 1.0 wt% xGnP; (d) 1.5 wt% xGnP. Figure S12: Experimental (symbols) and TS2 fit (lines) shift factors for 40HS polyureas with: (a) no added nanofillers; (b) 0.5 wt% xGnP; (c) 1.0 wt% xGnP; (d) 1.5 wt% xGnP; Figure S13: Experimental (symbols) and FMG–FMG fit (lines) master curves for IPDI-2k-20HS polyureas with: (a) no added nanofillers; (b) 0.5 wt% xGnP; (c) 1.0 wt% xGnP; (d) 1.5 wt% xGnP. Blue open circles represent storage modulus data and blue lines are the storage modulus model fits; orange open squares correspond to the loss modulus data and orange lines are the loss modulus model fits; Figure S14: Experimental (symbols) and FMG–FMG fit (lines) master curves for 30HS polyureas with: (a) no added nanofillers; (b) 0.5 wt% xGnP; (c) 1.0 wt% xGnP; (d) 1.5 wt% xGnP. Blue open circles represent storage modulus data and blue lines are the storage modulus model fits; orange open squares correspond to the loss modulus data and orange lines are the loss modulus model fits; Table S1: TTS reference temperatures and TS2 fit parameters for all systems.

Author Contributions: Conceptualization, D.A.T., M.Z. and V.V.G.; methodology, D.A.T., M.Z. and V.V.G.; validation, D.A.T. and A.K.; formal analysis, D.A.T. and A.K.; investigation, D.A.T. and A.K.; resources, D.A.T. and M.Z.; data curation, D.A.T. and A.K.; writing—original draft preparation, D.A.T. and A.K.; writing—review and editing, D.A.T., M.Z. and V.V.G.; supervision, M.Z. and V.V.G.; project administration, D.A.T.; funding acquisition, D.A.T. and M.Z. All authors have read and agreed to the published version of the manuscript.

Funding: This research was supported by the US Army Ground Vehicle System Center. A.K. and M.Z. were funded by the ARO Young Investigator Program (YIP) award (W911NF-19-1-0444) and the NSF award (DMS-1923201).

Institutional Review Board Statement: Not applicable.

Data Availability Statement: The data and analysis procedures are available from the authors upon request.

Acknowledgments: We thank Peter Askeland (MSU) for support with XPS measurements.

Conflicts of Interest: The authors declare no conflict of interest. The funders had no role in the design of the study; in the collection, analyses, or interpretation of data; in the writing of the manuscript; or in the decision to publish the results.

References

1. Sonnenschein, M.F. *Polyurethanes: Science, Technology, Markets, and Trends*; Wiley Series on Polymer Engineering and Technology; Wiley: Hoboken, NJ, USA, 2020; ISBN 9781119669463.
2. Szycher, M. *Szycher's Handbook of Polyurethanes*, 2nd ed.; CRC Press: Boca Raton, FL, USA, 2013; ISBN 9781439863138/143986313X/9781523108022/1523108029.
3. Akindoyo, J.O.; Beg, M.; Ghazali, S.; Islam, M.R.; Jeyaratnam, N.; Yuvaraj, A.R. Polyurethane Types, Synthesis and Applications–a Review. *RSC Adv.* **2016**, *6*, 114453–114482. [CrossRef]
4. Petrović, Z.S.; Ferguson, J. Polyurethane Elastomers. *Prog. Polym. Sci.* **1991**, *16*, 695–836. [CrossRef]
5. Koberstein, J.T.; Stein, R.S. Small-angle X-ray Scattering Studies of Microdomain Structure in Segmented Polyurethane Elastomers. *J. Polym. Sci. Polym. Phys. Ed.* **1983**, *21*, 1439–1472. [CrossRef]
6. Koberstein, J.T.; Galambos, A.F. Multiple Melting in Segmented Polyurethane Block Copolymers. *Macromolecules* **1992**, *25*, 5618–5624. [CrossRef]
7. Leung, L.M.; Koberstein, J.T. Small-angle Scattering Analysis of Hard-microdomain Structure and Microphase Mixing in Polyurethane Elastomers. *J. Polym. Sci. Polym. Phys. Ed.* **1985**, *23*, 1883–1913. [CrossRef]
8. Koberstein, J.T.; Leung, L.M. Compression-Molded Polyurethane Block Copolymers. 2. Evaluation of Microphase Compositions. *Macromolecules* **1992**, *25*, 6205–6213. [CrossRef]
9. Christenson, C.P.; Harthcock, M.A.; Meadows, M.D.; Spell, H.L.; Howard, W.L.; Creswick, M.W.; Guerra, R.E.; Turner, R.B. Model MDI/Butanediol Polyurethanes: Molecular Structure, Morphology, Physical and Mechanical Properties. *J. Polym. Sci. B Polym. Phys.* **1986**, *24*, 1401–1439. [CrossRef]

10. Ginzburg, V.; Bicerano, J.; Christenson, C.P.; Schrock, A.K.; Patashinski, A.Z. Theoretical Modeling of the Relationship between Young's Modulus and Formulation Variables for Segmented Polyurethanes. *J. Polym. Sci. B Polym. Phys.* **2007**, *45*, 2123–2135. [CrossRef]
11. Garrett, J.T.; Siedlecki, C.A.; Runt, J. Microdomain Morphology of Poly (Urethane Urea) Multiblock Copolymers. *Macromolecules* **2001**, *34*, 7066–7070. [CrossRef]
12. Garrett, J.T.; Runt, J.; Lin, J.S. Microphase Separation of Segmented Poly (Urethane Urea) Block Copolymers. *Macromolecules* **2000**, *33*, 6353–6359. [CrossRef]
13. Matsen, M.W.; Bates, F.S. Unifying Weak-and Strong-Segregation Block Copolymer Theories. *Macromolecules* **1996**, *29*, 1091–1098. [CrossRef]
14. Drolet, F.; Fredrickson, G.H. Combinatorial Screening of Complex Block Copolymer Assembly with Self-Consistent Field Theory. *Phys. Rev. Lett.* **1999**, *83*, 4317. [CrossRef]
15. Benoit, H.; Hadziioannou, G. Scattering Theory and Properties of Block Copolymers with Various Architectures in the Homogeneous Bulk State. *Macromolecules* **1988**, *21*, 1449–1464. [CrossRef]
16. Qi, H.J.; Boyce, M.C. Stress–Strain Behavior of Thermoplastic Polyurethanes. *Mech. Mater.* **2005**, *37*, 817–839. [CrossRef]
17. Kolařk, J. Simultaneous Prediction of the Modulus, Tensile Strength and Gas Permeability of Binary Polymer Blends. *Eur. Polym. J.* **1998**, *34*, 585–590. [CrossRef]
18. Bicerano, J. *Prediction of Polymer Properties*, 3rd ed.; CRC Press: Boca Raton, FL, USA, 2002; ISBN 0203910117.
19. Tzelepis, D.A.; Suzuki, J.; Su, Y.F.; Wang, Y.; Lim, Y.C.; Zayernouri, M.; Ginzburg, V. V Experimental and Modeling Studies of IPDI-Based Polyurea Elastomers—The Role of Hard Segment Fraction. *J. Appl. Polym. Sci.* **2023**, *140*, e53592. [CrossRef]
20. Velankar, S.; Cooper, S.L. Microphase Separation and Rheological Properties of Polyurethane Melts. 1. Effect of Block Length. *Macromolecules* **1998**, *31*, 9181–9192. [CrossRef]
21. Ionita, D.; Cristea, M.; Gaina, C. Prediction of Polyurethane Behaviour via Time-Temperature Superposition: Meanings and Limitations. *Polym. Test* **2020**, *83*, 106340. [CrossRef]
22. Ginzburg, V. A Simple Mean-Field Model of Glassy Dynamics and Glass Transition. *Soft Matter* **2020**, *16*, 810–825. [CrossRef]
23. Jaishankar, A.; McKinley, G.H. A Fractional K-BKZ Constitutive Formulation for Describing the Nonlinear Rheology of Multiscale Complex Fluids. *J. Rheol.* **2014**, *58*, 1751–1788. [CrossRef]
24. Jaishankar, A.; McKinley, G.H. Power-Law Rheology in the Bulk and at the Interface: Quasi-Properties and Fractional Constitutive Equations. *Proc. R. Soc. A Math. Phys. Eng. Sci.* **2013**, *469*, 20120284. [CrossRef]
25. Rathinaraj, J.D.J.; McKinley, G.H.; Keshavarz, B. Incorporating Rheological Nonlinearity into Fractional Calculus Descriptions of Fractal Matter and Multi-Scale Complex Fluids. *Fractal Fract.* **2021**, *5*, 174. [CrossRef]
26. Suzuki, J.; Gulian, M.; Zayernouri, M.; D'Elia, M. Fractional Modeling in Action: A Survey of Nonlocal Models for Subsurface Transport, Turbulent Flows, and Anomalous Materials. *J. Peridynamics Nonlocal Model.* **2021**, *5*, 392–459. [CrossRef]
27. Suzuki, J.L.; Zayernouri, M.; Bittencourt, M.L.; Karniadakis, G.E. Fractional-Order Uniaxial Visco-Elasto-Plastic Models for Structural Analysis. *Comput. Methods Appl. Mech. Eng.* **2016**, *308*, 443–467. [CrossRef]
28. Suzuki, J.L.; Naghibolhosseini, M.; Zayernouri, M. A General Return-Mapping Framework for Fractional Visco-Elasto-Plasticity. *Fractal Fract.* **2022**, *6*, 715. [CrossRef]
29. Suzuki, J.L.; Tuttle, T.G.; Roccabianca, S.; Zayernouri, M. A Data-Driven Memory-Dependent Modeling Framework for Anomalous Rheology: Application to Urinary Bladder Tissue. *Fractal Fract.* **2021**, *5*, 223. [CrossRef]
30. Winey, K.I.; Vaia, R.A. Polymer Nanocomposites. *MRS Bull.* **2007**, *32*, 314–322. [CrossRef]
31. Kim, H.; Abdala, A.A.; Macosko, C.W. Graphene/Polymer Nanocomposites. *Macromolecules* **2010**, *43*, 6515–6530. [CrossRef]
32. Ray, S.S.; Okamoto, M. Polymer/Layered Silicate Nanocomposites: A Review from Preparation to Processing. *Prog. Polym. Sci.* **2003**, *28*, 1539–1641.
33. Lin, C.-L.; Li, J.-W.; Chen, Y.-F.; Chen, J.-X.; Cheng, C.-C.; Chiu, C.-W. Graphene Nanoplatelet/Multiwalled Carbon Nanotube/Polypyrrole Hybrid Fillers in Polyurethane Nanohybrids with 3D Conductive Networks for EMI Shielding. *ACS Omega* **2022**, *7*, 45697–45707. [CrossRef]
34. Kausar, A. Polyurethane Nanocomposite Coatings: State of the Art and Perspectives. *Polym. Int.* **2018**, *67*, 1470–1477. [CrossRef]
35. Chen, K.; Tian, Q.; Tian, C.; Yan, G.; Cao, F.; Liang, S.; Wang, X. Mechanical Reinforcement in Thermoplastic Polyurethane Nanocomposite Incorporated with Polydopamine Functionalized Graphene Nanoplatelet. *Ind. Eng. Chem. Res.* **2017**, *56*, 11827–11838. [CrossRef]
36. Shah, R.; Kausar, A.; Muhammad, B.; Shah, S. Progression from Graphene and Graphene Oxide to High Performance Polymer-Based Nanocomposite: A Review. *Polym. Plast. Technol. Eng.* **2015**, *54*, 173–183. [CrossRef]
37. Albozahid, M.; Naji, H.Z.; Alobad, Z.K.; Wychowaniec, J.K.; Saiani, A. Thermal, Mechanical, and Morphological Characterisations of Graphene Nanoplatelet/Graphene Oxide/High-Hard-Segment Polyurethane Nanocomposite: A Comparative Study. *Polymers* **2022**, *14*, 4224. [CrossRef] [PubMed]
38. Kausar, A. Shape Memory Polyurethane/Graphene Nanocomposites: Structures, Properties, and Applications. *J. Plast. Film Sheeting* **2020**, *36*, 151–166. [CrossRef]
39. Ginzburg, V.V.; Hall, L.M. *Theory and Modeling of Polymer Nanocomposites*; Springer: Berlin/Heidelberg, Germany, 2021; ISBN 303060442X.

40. Meng, Q.; Song, X.; Han, S.; Abbassi, F.; Zhou, Z.; Wu, B.; Wang, X.; Araby, S. Mechanical and Functional Properties of Polyamide/Graphene Nanocomposite Prepared by Chemicals Free-Approach and Selective Laser Sintering. *Compos. Commun.* **2022**, *36*, 101396. [CrossRef]
41. Su, X.; Wang, R.; Li, X.; Araby, S.; Kuan, H.-C.; Naeem, M.; Ma, J. A Comparative Study of Polymer Nanocomposites Containing Multi-Walled Carbon Nanotubes and Graphene Nanoplatelets. *Nano Mater. Sci.* **2022**, *4*, 185–204. [CrossRef]
42. Balazs, A.C.; Bicerano, J.; Ginzburg, V.V. Polyolefin/Clay Nanocomposites: Theory and Simulation. In *Polyolefin Composites*; Wiley: Hoboken, NJ, USA, 2007; pp. 415–448. ISBN 9780471790570.
43. Fornes, T.D.; Paul, D.R. Modeling Properties of Nylon 6/Clay Nanocomposites Using Composite Theories. *Polymer* **2003**, *44*, 4993–5013. [CrossRef]
44. Bicerano, J.; Douglas, J.F.; Brune, D.A. Model for the Viscosity of Particle Dispersions. *J. Macromol. Sci. Rev. Macromol. Chem. Phys.* **1999**, *39C*, 561–642. [CrossRef]
45. Pinnavaia, T.J.; Beall, G.W. *Polymer-Clay Nanocomposites*; John Wiley & Sons, Ltd.: Chichester, UK, 2000.
46. Williams, M.L.; Landel, R.F.; Ferry, J.D. The Temperature Dependence of Relaxation Mechanisms in Amorphous Polymers and Other Glass-Forming Liquids. *J. Am. Chem. Soc.* **1955**, *77*, 3701–3707. [CrossRef]
47. Kennedy, J.; Eberhart, R. Particle Swarm Optimization. In Proceedings of the ICNN'95-International Conference on Neural Networks, Perth, WA, Australia, 27 November–1 December 1995; Volume 4, pp. 1942–1948.
48. Chen, X.; Wang, X.; Fang, D. A Review on C1s XPS-Spectra for Some Kinds of Carbon Materials. *Fuller. Nanotub. Carbon Nanostructures* **2020**, *28*, 1048–1058. [CrossRef]
49. Kwan, Y.C.G.; Ng, G.M.; Huan, C.H.A. Identification of Functional Groups and Determination of Carboxyl Formation Temperature in Graphene Oxide Using the XPS O 1s Spectrum. *Thin. Solid. Film.* **2015**, *590*, 40–48. [CrossRef]
50. Brune, D.A.; Bicerano, J. Micromechanics of Nanocomposites: Comparison of Tensile and Compressive Elastic Moduli, and Prediction of Effects of Incomplete Exfoliation and Imperfect Alignment on Modulus. *Polymer* **2002**, *43*, 369–387. [CrossRef]